Shape instabilities of islands in smectic films under lateral compression

Amine Missaoui, Kirsten Harth, Torsten Trittel, Christoph Klopp, Ralf Stannarius, Emmanuelle Lacaze

To cite this version:

Amine Missaoui, Kirsten Harth, Torsten Trittel, Christoph Klopp, Ralf Stannarius, et al.. Shape instabilities of islands in smectic films under lateral compression. Soft Matter, 2022, 18 (16), pp.3193-3205. ⟨10.1039/d2sm00144f⟩. ⟨hal-03713549⟩

HAL Id: hal-03713549
https://cnrs.hal.science/hal-03713549v1

Submitted on 10 Nov 2022

Shape instabilities of islands in smectic films under lateral compression

Amine Missaoui[a,b], Kirsten Harth[b,c], Torsten Trittel[b], Christoph Klopp[b], Ralf Stannarius[b], and Emmanuelle Lacaze[a]
[a] *Sorbonne Université, CNRS, Institut des Nanosciences de Paris (INSP), Paris, France.*
[b] *Institut für Physik, Otto-von-Guericke-Universität, Magdeburg, Germany.*
[c] *Fachbereich Technik, Technische Hochschule Brandenburg, Brandenburg a. d. Havel, Germany.*

Smectic liquid crystals are fluids, and in most rheological situations they behave as such. Nevertheless, when thin freely floating films of smectic A or smectic C materials are compressed quickly in-plane, they resist such stress by buckling similar to solid membranes under lateral stress. We report experimental observations of wrinkling and bulging of finite domains within the films, so-called islands, and give a qualitative explanation of different observed patterns. Depending on the external stress and the island dimensions, they can expel a specifically shaped bulge in their center, form radial wrinkles or develop target-like wrinkle structures. When the external stress is relaxed, these patterns disappear reversibly.

I. INTRODUCTION

A. Thin fluid films

Surface tension is the driving force of the shape relaxation of many fluid-fluid interfaces. It drives the relaxation of undulations or the retraction of deformed droplets to a spherical shape of minimal energy. This also applies to the shape relaxation of thin liquid films separating two fluids. A simple and well-known example are colorful soap bubbles, which enjoy grown-up humans often just as much as children. Their shape relaxation is in many respects similar to that of incompressible droplets (e.g. described in Refs. [1–6]). In contrast to droplets, neither the enclosed nor the surrounding fluid can be neglected in soap bubbles [7]. As long as the bubbles are large enough, the mass and inertia of the film are negligible, but the most important property of the thin liquid films is its viscosity that leads to an increased damping of bubble oscillations [7]. However, when the bubbles become small enough and the film mass is comparable to the enclosed air mass, the inertia of the fluid film must be taken into account [8, 9].

Flow of the inner and outer fluid will always couple to a redistribution of material in the film. The bubble shape relaxation is always coupled to flow in the separating film and thus a re-distribution of film material. In soap films of several square centimeters surface area, viscous effects or the redistribution of surfactant on the film surfaces can often be neglected. In smectic liquid crystal films, such a redistribution of film material is significantly hindered by the internal layer structure that inhibits thickness changes of the films. The latter involves a reorganization of the smectic layer structure. This process strongly affects the relaxation dynamics [10–14], both the shape changes of the relaxing bubbles and the surface area relaxation rates. The relaxation rate decreases both with increasing film thickness and with increasing homogeneity of the smectic film (decreasing number of layer steps present in the film) [12, 13]. The time scale of smectic layer reorganization sets the time scale of relaxation. Regarding rapid shape changes, such smectic bubbles possess an effectively zero dynamic surface tension, and the bending stiffness of the smectic layers for large-scale deformations is similarly low. Thus, the shape dynamics are reminiscent of lipid membranes and vesicles. External forcing can cause, e.g., wrinkling or bulging instabilities of these bubbles [10, 11, 14].

Rheological properties which strikingly alter the dynamic behaviour of thin films in rapid processes, i.e. during changes which occur much faster than the relaxation time scale of the films, have also been observed in rupture events: In soap films with immobile surfactants [15] or extremely thin (Newton black) films [16], sudden cracks appear around the growing hole in the film, and retraction slows down. Collapsing bubbles of very viscous liquids wrinkle under the action of gravity [17]. When a viscous drop creates a thin spread-out film in a crater during impact on a liquid pool, such films can wrinkle transiently [18]. This phenomenon is reminiscent of elastic sheets under external stress. Note that sufficiently visco-elastic fluid filaments can also exhibit dynamic buckling upon compression or rupture [19, 20]. As extreme cases, one may consider deformations of lipid or cell membranes or vesicles, whose dynamics on short time scales is dominated by bending rigidity instead of surface tension [21]. This can cause wrinkling or the extrusion of tubuli upon lateral membrane compression [22–25]. All these structures are transient, the relevant parameter is the separation of time scales of film or filament relaxation compared to that of the external stresses acting on the membrane. Here, we identify, analyze and describe patterns in local regions with excess smectic layers (so-called islands) in smectic films. They can develop shape instabilities under compression even while the surrounding film still remains plane. We show that this is related to the line tension of the islands. Their morphologies closely resemble similar patterns described in thin solid sheets, as detailed in the following section.

B. Wrinkling of solid sheets

The classical, and most investigated system exhibiting wrinkles consists of joint solid multilayers with incommensurate elastic properties under lateral stress. This is encountered, e.g. in drying fruit [26], but also in oxidized surface layers of PDMS, or thin incommensurate crystalline structures [27]. A second scenario is stress response in thin elastic membranes (without elastic substrate): This includes, e.g., stretched clamped or poked sheets [26, 28], thin elastic sheets on a liquid surface [29, 30], or the response of an elastic sheet that has an excess size compared to the shape enforced by external constraints. Wrinkled curtains [31], or wrapping problems where a planar sheet is externally forced into a curved shape have been described [32–34]. In contrast to the *dynamic* wrinkling instabilities in fluids as mentioned in the introduction, most of these patterns in elastic layers concern *static* wrinkling and buckling. There is no relevant relaxation in the structures. The deformations resemble equilibrium structures. Wrinkling caused by highly *dynamic* external forcing can occur as well, but is less investigated. A recent study models wrinkles caused by a particle impacting onto thin elastic sheets floating on a water bath [35].

Different wrinkle morphologies are observed depending on the stress and excess area of the membrane. Chung et al. [36] crosslinked the surface of thin polystyrene films and swelled the remaining non-crosslinked part of these films with toluene afterwards. Near local impurities or defects in the solid surface layer, they observed two types of radially expanding wrinkling patterns, one with radial undulations, the second one with circular ones. They identified different crosslinking times as the cause for the appearance of these different wrinkling morphologies.

Similar structures have been found in numerous other experiments when a thin solid membrane is exposed to in-plane stress by viscous flow, deformations of attached layers of elastic material, indention or other methods. Zhao et al. covered a shape-memory polymer with a thin gold layer and described different wrinkle morphologies upon temperature changes as a consequence of thermal expansion mismatches between the gold and polymer layers [37]. This and similar reports are interesting in the context of the present study because of the close resemblance of the structures described there and the patterns we observe in islands of freely floating smectic bubbles. Figure 1 shows in the top row two images of the polymer/gold film stack after shape recovery of the polymer material. In the left image, the polymer was treated such that it forms a protrusion after thermal recovery, and a radial ray-like pattern is produced. In the right image, the gold film wrinkles in a circular target-like pattern. The bottom row shows selected smectic islands on a freely floating bubble subject to rapid external forcing.

C. Wrinkling of smectic freely floating films

In the present study, we describe deformations of freely floating bubbles whose membrane consists of fluid material in a smectic C liquid crystalline phase. The layered structure of the films inhibits a fast reduction of the film area and consequently a fast shape relaxation of non-spherical bubbles. This can increase the typical relaxation time from tens to several hundreds of milliseconds [10–13]. While surface tension drives the global bubble shape relaxation, it is practically irrelevant for shape changes on short time scales. Recently, regular film undulations as a consequence of local in-plane compression of the films by external forcing were reported [12, 14, 38] and their morphology was described. This phenomenon was explained with a simple model as a transient *dynamic* buckling instability [14]. The growth rates of unstable undulation modes determine the wavelength selection. Short wavelength modes are suppressed by the elastic forces related to deformations of the smectic layers, while long wavelengths grow slower because they require the redistribution of the outer fluid (air) over longer distances. The relation between wrinkle wavelength and film thickness under isotropic compression was recently measured employing the geometry of collapsing catenoids with a film in the waist [38]. In freely floating smectic bubbles, converging flow of the surrounding air was identified as the driving external force compressing the local surface area [14], but the actual compression rates are usually hard to determine. In such bubbles, a second scenario of stress relaxation was observed, viz. the bulging of thicker patches (islands) on the bubble surface [11, 12, 14], as well as the extrusion of tubuli and a constriction of buds [10, 11]. Their formation has been qualitatively explained by the presence of the well-known line tension due to the layer dislocations around the perimeter of the island, but neither the origin of their characteristic shapes nor quantitative measurements of the instability have been addressed yet.

In addition to the analysis of bulge shapes, we discuss certain wrinkling patterns which appear exclusively within islands in freely floating smectic films subject to lateral compression by external forces. The bottom row in Fig. 1 shows two examples. These localized undulations exhibit striking similarities to patterns formed in thin elastic sheets [35–37, 39]. We adapt a model initially developed for wrinkling instabilities of freely-floating bubbles with uniform thickness [14] to localized instabilities of smectic islands. The island size and thickness as well as the line tension of its border are key parameters for the pattern formation and wavelength selection.

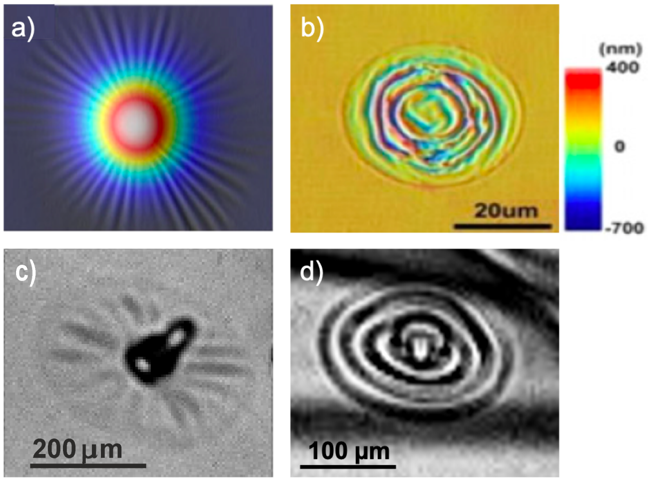

Figure 1. Top: Images of gold coated shape memory polymers after shape recovery of a locally indented sample. a) Radial pattern above a protrusion of the shape-recovered polymer, b) Ring pattern above a pre-indented area. Images (a,b) are reproduced from Zhao et al. [37] with permission, copyright IOP Publishing. Bottom: Wrinkling structures observed in smectic islands. c) radial undulations around a tubulus formed perpendicular to the film, d) tangential undulations of a nearly flat island.

II. MATERIALS AND METHODS

Here, we report observations in microgravity on freely floating smectic C bubbles made of a mixture of equal volumes of 5-n-octyl-2- [4-(n-hexyloxy) phenyl]pyrimidine and 5-n-decyl-2- [4-(n-octyloxy) phenyl]pyrimidine (both commercially available from Synthon Chemicals). This mixture exhibits a smectic C phase at room temperature up to 52° C, followed upon heating by smectic A phase ($T_{\rm CA} = 52^\circ$) and a nematic phase ($T_{\rm AN} = 68^\circ$) before the isotropic phase is reached ($T_{\rm NI} = 72^\circ$). The mixture has a surface tension of 22.45 mN/m at room temperature [10].

Freely floating bubbles were created by a technique described in earlier works [10, 40], as sketched in Fig. 2: A small amount of about 1 mg of the smectic material was introduced between two coaxial circular metallic rings ($R_{\rm ring}$ = 25 mm inner radius), which were thereafter brought into contact. Using a stepper motor, the rings were then slowly separated from each other, so that a catenoid-shaped smectic film formed. Above a critical separation between the rings, $D_{\rm crit} \approx 1.3254\ R_{\rm ring}$, the catenoid-shaped film collapses. Mainly because of its inertia, some of the air inside the catenoid is trapped between the two pinch-off points, and an elongated bubble is formed [41]. The bubble oscillates for a few dozen milliseconds until it reaches the stable spherical shape with minimal film surface.

The equilibrium radii of these bubbles are of the order of $R \approx 3$ mm. The exact radius in individual experiments depends slightly on film thickness, temperature and other parameters [10]. In addition to this bubble, there are often two oscillating films remaining in the catenoid rings, whose oscillations cause motion in the air surrounding the bubble and generate an external force on the relaxing bubble [11]. Alternatively, the bubble can also be submitted to external forces with acoustic waves generated by two loudspeakers implemented behind the catenoid support rings. Then, one has the advantage to control the excitation phases and frequencies.

We study the fast dynamics of islands on the bubbles during the comparably slow phase of shape relaxation after the pinch-off, before the bubbles reach their spherical equilibrium shape. As soon as the sphere shape is reached, neither the oscillating remnant films nor the loudspeakers included in our setup are able to cause noticeable shape changes of the bubble.

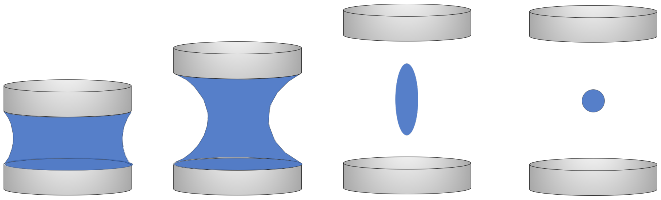

Figure 2. Sketch of the procedure to prepare freely floating smectic bubbles using catenoid collapse.

The smectic catenoid is back-illuminated by either white or monochromatic parallel light using white and blue (wavelength 460 nm) LEDs. The catenoid collapse takes place within less than a few milliseconds (see, e.g., Ref. [38]). We use a high speed camera (Phantom VEO 710) equipped with a commercial Canon lens. The typical recording speed is 7500 fps with a spatial resolution of approximately 5 μm/pixel. It is focused onto the film of the bubble facing the camera (front side) with high magnification to ensure that details of the island dynamics can be acquired. However, it is not possible to observe the global shape of the bubble and the details of the surface dynamics with sufficient resolution on the same images. Thus, a GoPro Hero action camera at a recording speed of 120 fps is implemented at 90° with respect to the Phantom camera and to the catenoid symmetry axis in order to acquire the global view of the bubble during the oscillation. The thickness of the background film (the uniformly thick film around potential islands) equals that of the catenoid from which the bubble was generated. For simplicity, we usually determine the film thickness in the moment of the catenoid collapse when the central part assumes a roughly cylindrical shape. Images are normalized by the background prior to extraction of transmission intensity values. We average over several profiles at equal radius in order to reduce noise. Subsequently, the film thickness is determined by fitting background-corrected intensity profiles [42] assuming an effective refractive index of 1.53 of the smectic material. This value is known for homologues of our mixtures. The approximate thickness of selected islands was determined from their transmission intensity, considering their position and the background film thickness of the bubble [43]. Typical background film thicknesses are around 20 nm, islands can be significantly thicker. The thickness of individual smectic layers is approximately 2.7 nm at 25 °C [44].

Under normal gravity conditions, the initial shape of the bubble just after pinch-off is asymmetric [10]. It often pinches off at the upper end first , and this, in turn, influences the oscillation behavior. In addition, since it is a freely floating bubble, it is difficult to keep it in focus; it quickly moves out of the focal plane and can even leave the observation window of the optical microscope prior to reaching the sphere shape. Hence, it is difficult to study island dynamics in normal gravity experiments. For this reason, most of the experiments were performed under microgravity conditions during the VP148 CNES parabolic flight campaign at NOVESPACE (Bordeaux, France), and previous DLR campaigns with the same provider.

III. FILM AREA REDUCTION

Due to the incompressibility of the smectic liquid, a lateral compression of the smectic film in general requires a local increase of the film thickness. A stress-induced reduction of the tilt angle of the SmC phase [45] can only transiently compensate a small fraction of the required surface area reduction. Islands typically form already during catenoid collapse. During bubble shape relaxation, these islands grow and accommodate the excess material from the background film during the reduction of the surface area of the smectic bubble [10, 11]. They act as reservoir of material, similar to the meniscus in frame-supported films. The island growth is achieved by excess smectic material from the surrounding film that is adsorbed at the island circumference. After the bubble shape relaxation, the rapid growth of islands ceases, and only long-term equilibration processes such as coalescence and Ostwald-ripening on the bubble will take place [46].

The islands are surrounded by layer dislocations. The geometry of such an island on a smectic bubble is sketched (much exaggerated) in Fig. 3b. One cannot see the dislocation loops directly in an optical microscope as their size is well below the resolution limit. What is seen is the boundary between regions of different thickness, which in general have different optical transmission intensities and are identified by their optical contrast. In Fig. 3, islands can be identified as darker spots. Their brightness is directly related to the local film thickness which finally allows for their thickness determination [14, 40, 42].

On average, some 30 to 40 islands formed on each bubble. They can interact with each other and in some cases, the islands can even merge when they get in contact. Despite its importance and a general interest in the coalescence phenomenon [47–49], this feature will not be analyzed here. We have chosen islands that are isolated and sufficiently far from neighboring ones to avoid coalescence during the analysis of dynamics. Depending on their position and orientation on the bubble surface respective to the optical axis of the camera lens, any island that lies in a plane forming an angle other than 90° to the optic axis appears deformed in the perspective view. For the interpretation of measurements of the islands dynamics, we assume that the islands remain nearly circular. Then, the long axis of the projected ellipse represents the actual island radius r.

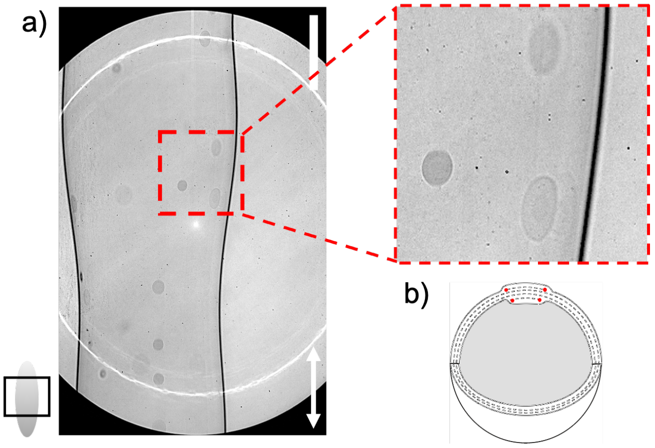

Figure 3. (a) Islands (darker regions) on a freely floating smectic bubble. The equilibrium radius of the bubble is R ≈ 2.7 mm. The black square on the sketch of the bubble in the bottom-left corner indicates the field of view of the camera. The white bar represents 1 mm. The axis of symmetry of the catenoid is indicated by the white arrow. (b) Sketch of a cut through a smectic bubble. The smectic layers are indicated by dashed lines. In the upper part, the cut through an island is shown, with the layer dislocations marked by red dots.

The dynamics was studied in about 80 smectic islands in 70 shape-relaxing bubbles. The relaxation of the bubble is associated with a slow decrease of the film surface area, thus we observe a systematic increase of effective island areas, i.e. the projection of the surface of the island onto the plane of the surrounding film, until the spherical equilibrium shape of the bubble is reached. Thicker islands grow more slowly than thinner ones. This is in agreement with previous results [10, 11].

However, for 25 out of 80 investigated islands, we found an unexpected behavior: The island radius temporarily ceases to grow to finally join back the initial growth curve after some time, as exemplarily shown in Fig. 4a,b. Fig. 4a shows an island during the axial compression and dilation of the bubble induced by the films in the holder rings that oscillate in anti-phase with a frequency of approximately 16 Hz. The sudden change of island projection growth occurs during the compression period. Fig. 4c,d show that during this period, the island forms a bulge first, and a tubulus later during the maximum compression. The formation of bulge and tubulus reduces the effective island area as seen in the graph. When the compression period has finished, the island returns to its original flat shape (Fig. 4e). The observation that the island radius evolution joins back to the initial growth curve in Fig. 4a indicates that during this reversible deformation, the actual surface area of the island grew continuously, and it continues to grow further until the bubble reaches the spherical shape.

Figure 4 b shows an island during the repeated axial compression and dilation of the bubble by means of an acoustic excitation with two loudspeakers placed behind the film holders. The loudspeakers work in antiphase at a frequency of 120 Hz, so that the bubble is repeatedly compressed in axial direction every 8.33 ms. Figures 4f-h depict the bulged island during the first compression, the flat island during axial dilation of the bubble and the repeated bulging during the next compression phase. The effective island area is consequently decreasing twice in the graph.

IV. BULGING OF SMECTIC ISLANDS

As is seen in Fig. 4, an effective reduction of the lateral island extension can be achieved with the very simple extrusion of protuberances of different shapes out of the film plane. One might naively assume first that these protuberances are bell or dome shaped. In fact, we observe bulges of very different shapes, but in most cases they have very characteristic appearances. Some examples are shown in Fig. 5 a,b. There is a simple reason for the selection of these shapes: sphere caps, cones, cylinders capped with a hemisphere and other, more complex geometries. These shapes have one property in common: they are composed of cylindrical, conical and circular segments (Fig.5 c). A characteristic feature of these shapes is that they locally preserve the smectic layer spacing. Distortions of the film shape that involve local changes of the smectic layer spacing (e.g. sine undulations that are discussed in the next section) are inhibited by the comparably large smectic layer compression modulus B. The elastic energy needed for layer compression grows with the fourth power of undulation amplitudes and the fourth power of the wave number of undulation modes. Therefore, dilation has an influence particularly for deformations on small scales. For large deformation amplitudes, avoiding layer dilation or compression is an important aspect of energy minimization. Elastically driven spontaneous layer undulations in smectic C menisci [50–52] can be explained following a similar shape selection of circular arc segments [53].

Even though we do not expect to find equilibrium shapes during the dynamical evolution of the protuberances within the islands, they grow slowly enough to avoid deformations which lead to a local compression or dilation of the smectic layers: Thus, the protuberances have their characteristic shapes. For example, the cylinder-shaped protrusion shown in Fig. 6 that has formed during the lateral compression phase of the film relaxes during the subsequent expansion of the local film region by only reducing its length, keeping the tube diameter constant at about 45 μm (see the 3rd scheme on Fig. 5c). It is located in some terraced smectic island which is larger than the image shown and remains flat otherwise. At its maximum extension, the

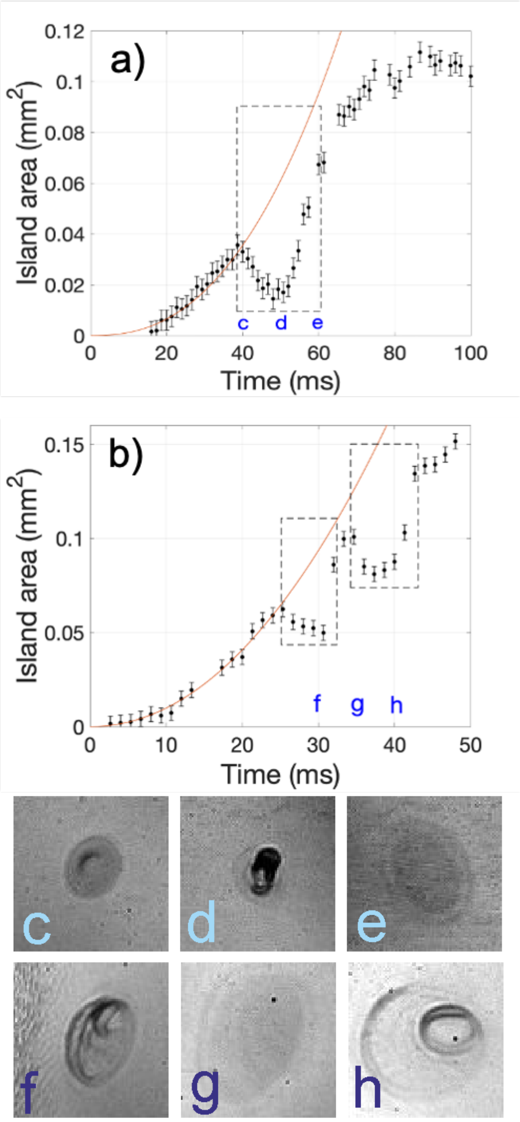

Figure 4. Growth of the effective island area (plane area surrounded by the island border) as a function of time in two examples (a,b). The sharp drops are indicated by the black dashed squares. The solid red line is a quadratic fit. See text for more explanation. These islands form protrusions, which can effectively expel smectic material out of the film plane. Images (c-e) and (f-h) show the shapes of the islands in different phases of compression for the island of graph (a) and (b), respectively. Time stamps refer to the start of recording. Image sizes are 350 μm ×350 μm.

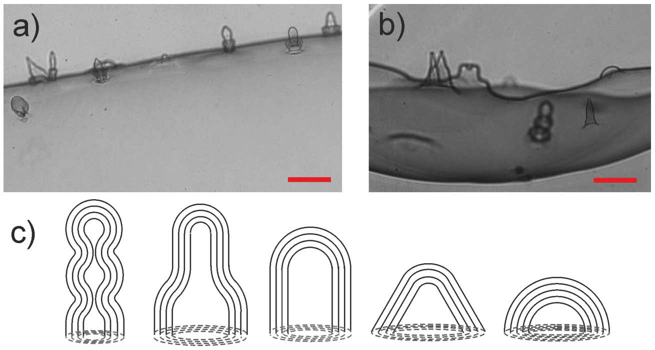

Figure 5. a,b) Bulges of different shapes growing within smectic islands during a local lateral film compression. Scale bars mark 0.2 mm. c) Sketches of cross sections of some typical shapes of protrusions where the smectic layers of constant period are seen.

protrusion is 0.23 mm long and contains a film area of roughly 0.03 mm^2, this is about 5 % of the surrounding island area.

When the compression phase persists long enough (several milliseconds), long tubes can exhibit some kind of Rayleigh-Plateau instability and develop axial modulations of their radii. They may then irreversibly transform into spherical partitions (see Fig. 5b and first scheme on Fig. 5c).

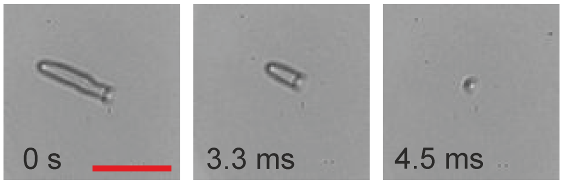

Figure 6. A single tube-shaped protrusion relaxes after the film region is dilated again. The scale bar marks 0.2 mm.

V. WRINKLING OF SMECTIC ISLANDS

The reversible sudden drop of the effective island area may not only be related to bulges as seen in Fig. 4, but also to wrinkles inside the islands. Fig. 7a shows optical images of the gradual formation of circular wrinkles within an island during the identified drop of the effective island area (Fig. 7d). These wrinkles are film undulations that represent an alternative way for decreasing the effective island area under lateral compression (see Fig. 11 below). Figure 7b presents the intensity profiles of these images measured along a line drawn across the island (see red dashed line in Fig. 7a). The wrinkles are characterized by the selection of a wavelength λ. For this exemplary island, the wavelength is $\lambda \approx 40 \pm 5$ μm at $t = 72.5$ ms.

Figure 7c shows the space-time plot measured along a material-fixed equatorial line drawn across the island. Note that the dark lines parallel to the radial coordinate axis at about $t = 70$ ms are artifacts of a crease of the film at the rear side of the bubble, see Fig. 8. The wrinkles typically form near the center of the island first. Afterwards, new wrinkles appear further away from the center as shown by the dark and bright lines parallel to the time axis starting one after the other. This process is accompanied by a simultaneous small reduction of the wavelength, λ, of approximately 15% between $t = 49$ ms and $t = 72$ ms. The actual surface area of the film inside the island continues to grow during the formation of the wrinkles. This is evident from the wrinkles increasing of their amplitudes and also from new undulations being formed. This observation is qualitatively consistent with

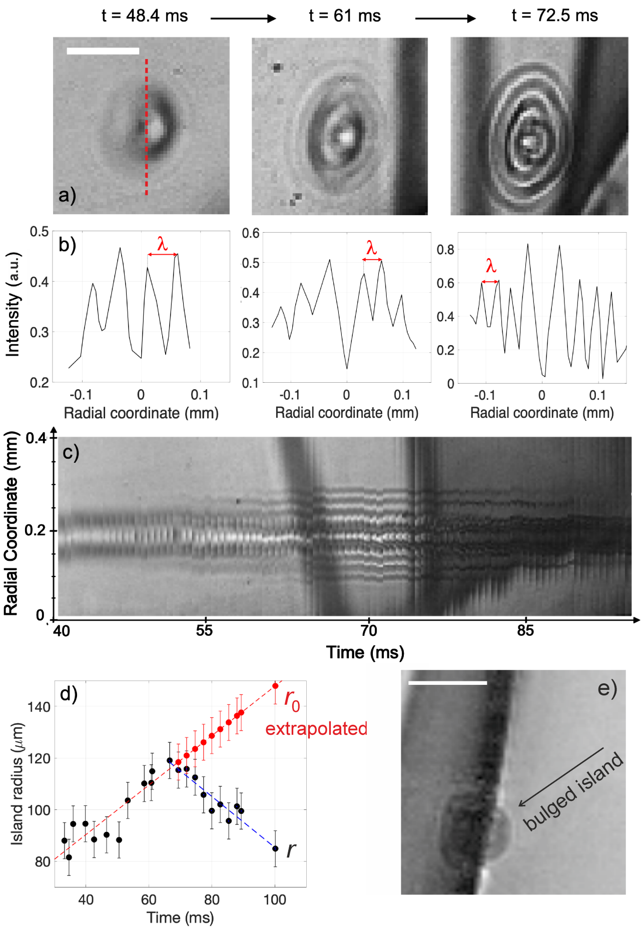

Figure 7. (a) Formation of ring-shaped wrinkles within an island. (b) Wrinkle intensity profile plot along the red line as a function of time. (c) Space-time plot showing the dynamic behavior of wrinkles with time. Wrinkles appear near the island center first, then new undulations gradually appear at the outside, seen as dark and bright lines parallel to the time-axis. (d) Radius of the island shown in Fig. 7(a) as a function of time. The red dots are a linear extrapolation of the radius $r_0(t)$. (e) Side view of the same island before it leaves the field of view. The deformation has reached an amplitude of ≈ 70 μm. White bars in (a) and (e) represent 100 μm.

the increasing optical contrast in Fig. 7b. Between $t =$ 48.4 ms and $t = 72.5$ ms, the contrast modulations almost double.

Black symbols in Fig. 7d show the time-dependent radius of the island of Fig. 7a, *r(t)*. It increases monotonously with time before wrinkles form. At approximately $t = 60$ ms, well-defined regular circular wrinkles appear within the island and the growth of the outer island radius, *r(t)*, is reversed. Without wrinkles, the true radius $r_0(t)$ of the island would follow the extrapolated previous trend, sketched by the red dots in Fig. 7d. The difference between the actual radius r of the island and the extrapolated in-plane radius r_0 provides a compression rate defined as $\Gamma = \mathrm{d}(r(t) - r_0(t))/\mathrm{d}t$. The linear fit in Fig. 7d for data after 60 ms, shows that Γ remains on average constant over time, with a mean value of about $2{\pm}0.3$ μm/ms. We note that the wrinkles in this particular island slowly coarsen to form a kind of sphere cap (Fig. 7e at $t = 113$ ms) before the island left the field of view. The background film plane has slowly rotated in this bubble region so that the image shows almost the side view of this bulge.

The fact that the wrinkle patterns appear with a certain delay and not just after pinch-off can be attributed to the fact that the bubble is axially compressed by two remnant films in the ring holders which oscillate in antiphase (with a frequency of about 16 Hz). Harth et al. [14] have demonstrated that the surrounding airflow generated by these films can induce an axial compression of the bubble. This external forcing is the main reason for wrinkling of the smectic satellite bubble itself [14]. External disturbances are often associated with complex shapes that smectic bubbles can acquire during the oscillation phase. Figure 8 sketches the region where the island studied in Fig. 7 is observed (indicated by the black arrow). This particular island was found close to a complex invagination of the bubble appearing at its top. When such complex regions appear, they can cause a local compression of the film area, which in this case induces not only wrinkles within the island but also in the surrounding film region (indicated by the circle in Fig. 8).

Fig. 9 shows a typical image sequence of a contracting section of a relaxing bubble, randomly speckled with islands. In order to visualize the axial contraction of the bubble, we marked two islands (at $t = 27$ ms) by solid arrows. In the following two images, we show the shift of their instantaneous positions (open arrows) with respect to the initial one (solid arrows). The difference between the solid and open arrows indicates an axial contraction of the bubble section. The local area of the displayed region remained nearly constant.

The bubble section of Fig. 9 shows that islands of similar thickness react to lateral compression in different ways: While the large island (marked in blue) grows without developing any visible wrinkles, the intermediate (marked in black) and small island (marked in red) are both affected by the compression. The intermediate

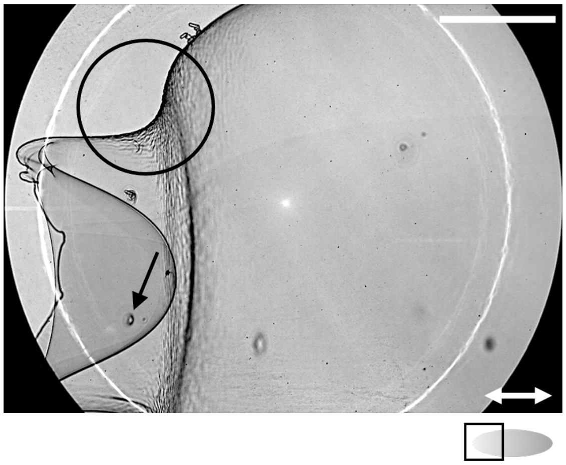

Figure 8. Complex shape acquired by the freely floating bubble during the oscillation regime. Film wrinkles formed close to the deformed region of the film shown by the black circle. The arrow points at the island studied in Fig. 7. The white bar represents 1 mm. The symmetry axis of the catenoid is indicated by the white double-arrow. The black square on the sketch of the bubble in the left image indicates the field of view of the camera.

island develops ring-shaped wrinkles similar to the pattern observed in Fig. 7. The wrinkles in that island appear around $t = 35$ ms, and a preferred wavelength is selected. The small island forms a single bulge at the center approximately 8 ms before the medium island becomes unstable. We conclude that the size of the island is an important parameter for wrinkle formation.

We note that radial wrinkles can be observed as well. They are systematically connected with the presence of a small bulge in the island center. Figure 10 shows a typical example of star-shaped wrinkles, where radial undulations are formed within the island surface. This scenario begins with the formation of a central bulge, approximately 25 ms after pinch-off. This bulge grows slowly under the action of a continuous compression. The relatively constant base diameter of this bulge of about 45 μm is maintained because the island contained an even thicker central plateau. After about 53 ms, radial wrinkles appear. They reach their maximum between 58 ms and 67 ms. Then, the wrinkling pattern flattens again within 3 ms after the compression phase ended. The bulge persists for another 65 ms, slowly shrinking, until the island is flat again.

VI. WRINKLING ISLAND MODEL

The spontaneous undulation of layers in liquid crystal samples has been known since about 50 years. Originally, the model was developed for cholesteric samples distorted by external electric or magnetic fields by Helfrich [54] and Hurault [55], the deformation is thus known as Helfrich-Hurault instability. Delaye et al. [56] first

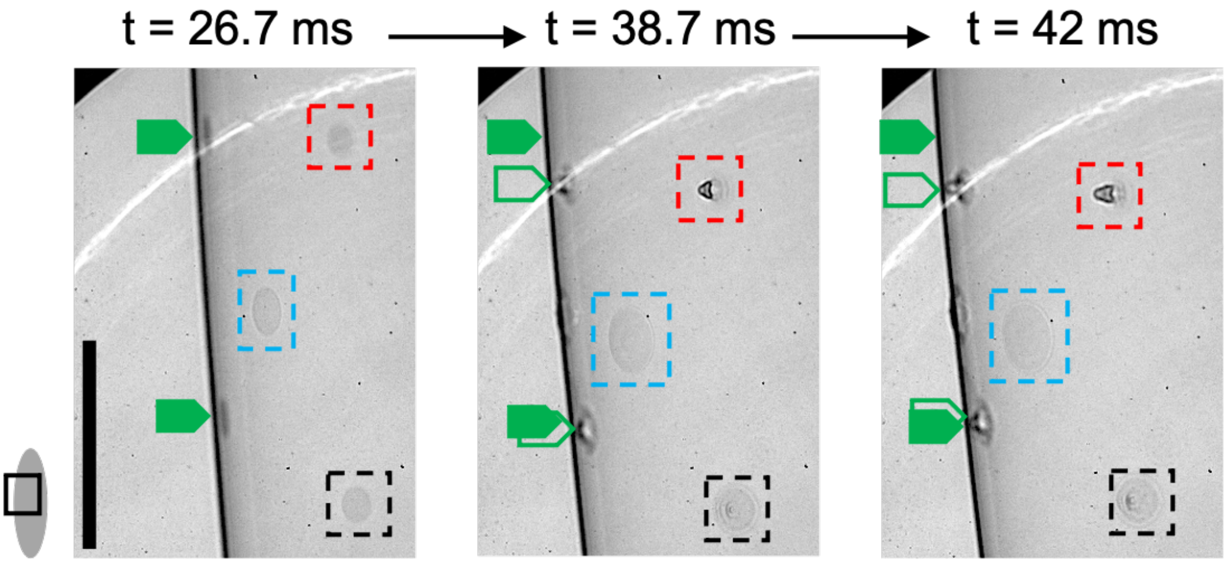

Figure 9. Size-dependence of the response in similarly thick islands to external compression: The solid green arrows mark the initial position of two islands near the side of the bubble, and are copied to images at later times. The current position of these islands is marked by empty arrows. The difference indicates the axial compression. While the background film and the large island (marked by the blue square) remain flat, a medium-sized island (black square) wrinkles and a smaller island bulges (red square). Time counts from the beginning of the recording, which started few milliseconds before pinch-off of the bubble. The black bar represents 1 mm. Bubble thickness ≈ (18 ± 3) nm.

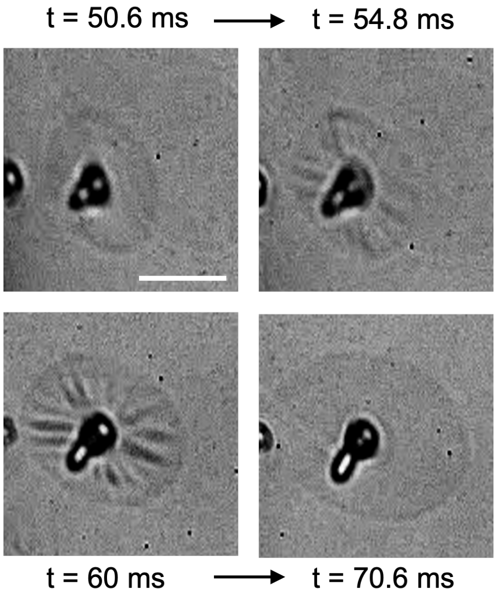

Figure 10. Formation of a tubulus in the center of an island. The detachment of such a tubule creates a stress that causes the island to wrinkle as shown at $t = 57$ ms. Time counts from the beginning of recording, which started few milliseconds before pinch-off. The white bar represents 200 μm.

described this undulation in a smectic A cell with homeotropic boundary conditions (layers in the cell plane) under dilational stress normal to the cell plane. A review of this instability has been published by Blanc et al. [57]. In Delaye's experiment, the cell plates were displaced so that the cell thickness was slightly enlarged. The smectic layers develop undulations to compensate the cell thickening, seeking a compromise between elastic energies for splay deformations and layer dilation.

The situation is quite different from our geometry because the top and bottom layers in the cell are assumed to remain flat, while in the present freely floating films the undulations are uniform across the film. Menisci of SmC and (partially) SmA films can also display spontaneous layer undulations [50–52] originating from elastic interactions between local orientations and curvature of the layers [53]. In that model, the undulations consist of circular arc segments, avoiding layer dilation or compression. Thin free-standing films are usually flat because of the action of the surface tension. For the wrinkles in smectic films under rapid compression [14, 38], i.e. the situation considered here, surface tension can be neglected.

Harth et al. [14] have developed a one-dimensional model to describe the wrinkle structures in freely floating smectic bubbles and to estimate the value of the selected wavelength. This model can be adapted to the case of circular islands, taking into account the line tension of the surrounding dislocations. The surface area of the island is considered to be compressed by external compressive forces, $\vec{F}_s$, considered as dispersed along the island perimeter (Fig. 11). The corresponding mechanical work, W_s, in the radial configuration of the wrinkling island is therefore:

$$W_s = 2\pi r(r_0 - r)F_s, \tag{1}$$

with F_s the force per unit of length. The response of the film is the formation of wrinkles with initial wavelength λ_0 and amplitude *a(t)*. The initial wave number is $q_0 = 2\pi/\lambda_0$. We approximate the wavelength, λ, to be fixed during the wavelength selection process, and $q \approx q_0$. The temporal variation in the experiments is indeed only of about 15 %.

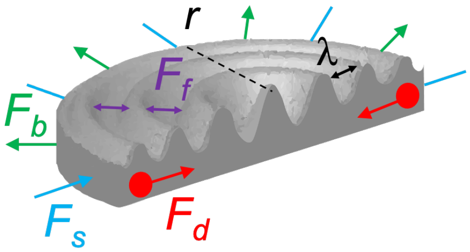

Figure 11. Sketch of a wrinkling circular island showing the applied forces. The red circles indicate the dislocation lines surrounding the island. λ is the wrinkles characteristic wavelength.

The circular geometry of the island and the presence of a ridge in the center of the island, as shown in Fig. 7, strictly does not allow to describe the radial deformation by harmonic functions. An ansatz with Bessel functions would be more consistent. However, for a simplified model, one may approximate the radial deformation of the undulated island by a linear ansatz: $u(r) = a\cos qr$, with $q = 2\pi/\lambda$. The surface area of the island in the absence of wrinkles is: $A = \pi r_0^2$. In the presence of wrinkles, the surface area can be obtained in the cylindrical coordinate system as

$$A = 2\pi \int_0^r \sqrt{1+u'^2}\rho \mathrm{d}\rho \approx \pi r^2(1+\frac{a^2q^2}{4}) \tag{2}$$

where the integral is over the radial coordinate ρ relative to the island center. Thus, we obtain

$$r_0 \approx \sqrt{1+\frac{a^2q^2}{4}}\, r \approx (1+\frac{a^2q^2}{8})\, r, \tag{3}$$

for weak undulations. Therefore, the mechanical work performed by the compressive force, W_s, can be written as

$$W_s = f_s \frac{\pi r^2}{4} a^2 q^2. \tag{4}$$

In the experiments shown above, where islands are speckled on the bubble surface, wrinkles appear inside these islands but not on the background film of the bubble itself. The island diameter is an important parameter. We thus assume that the line tension of the dislocations in the island border supplies a crucial contribution to the compressive stress which finally triggers the instability.

The line tension of the island border with dislocations, γ, plays a role similar to F_s, with a positive work when the island perimeter decreases. Its mechanical work can be written as: $W_d = 2\pi(r - r_0)\gamma$, therefore

$$W_d = \gamma \frac{\pi r}{4} a^2 q^2. \tag{5}$$

Naively, we assume for now that γ is the static line tension that can be measured in experiments [47, 48, 58, 59]. This issue will be discussed in detail below. It is related to the line tension of a single dislocation, γ_s, and the number of layer steps at the island boundary, by $\gamma = N\gamma_s$

The bending of smectic membranes induced by the wrinkles leads to an elastic free energy density contribution of the form [14]

$$\mathrm{w}_b \approx \mathrm{w}_{\mathrm{elastic}} = \frac{K_{11}}{2} a^2 q^4 \cos^2 qr, \tag{6}$$

with the constant K_{11} for splay deformations of the director $\vec{n}$. It should be noted that this model is strictly valid for films in the smectic A phase. Here, we consider it applicable as well because it has been demonstrated earlier [45] that a quick lateral shrinkage of thin smectic C films induces a transition into smectic A. We assume that the tilt angle is reduced by the lateral compression so that a smectic A model is appropriate.

The mechanical work associated with the bend of the smectic layers can be derived similarly to the model by Harth et al. [14], with the average $\overline{\cos^2 qr} = 1/2$, as

$$W_b = \frac{K_{11}\pi r^2 h}{4} a^2 q^4, \tag{7}$$

where h is the island thickness.

Another possible elastic energy contribution mentioned already in the previous section is related to the smectic layer compression in an undulated film. In a purely sinusoidal model with small amplitudes, this compression is $(1 - \cos\varphi)$ with $\varphi = aq\sin qx$ being the angle of the layer plane respective to the undistorted film.

The energy density corresponding to layer compression or dilation can be obtained as

$$w_c = \frac{1}{2} B(1-\cos\varphi)^2, \tag{8}$$

where B is the smectic layer compression modulus. Expanding the cosine function as $\cos z \approx 1 - z^2/2$ yields

$$w_c \approx \frac{B}{8}\varphi^4 = \frac{B}{8} a^4 q^4 \sin^4 qr. \tag{9}$$

Applying the spatial average $\langle \sin^4 qr \rangle = 3/8$, we obtain

$$W_\mathrm{c} + W_b \approx \pi r^2 h \left(\frac{3}{64} B a^4 q^4 + \frac{1}{4} K_{11} a^2 q^4 \right) \qquad (10)$$

The contributions of both terms, W_c and W_b, relate as

$$\beta = \frac{W_\mathrm{c}}{W_b} = \frac{3B}{16K_{11}} a^2. \qquad (11)$$

Which of them is important depends upon the magnitude of a, and we use the rough estimate $K_{11}/B \approx d_0^2$ that relates the ratio of the two elastic constants to the order of magnitude of the smectic layer thickness d_0, thus

$$\beta \approx \frac{3\,a^2}{16\,d_0^2}. \qquad (12)$$

When one considers initial fluctuations with the thermal energy $kT \approx 4 \cdot 10^{-21} J$, it can be seen that the layer compression term (scaling with a^4) is negligible in our model. Thus, we can safely rely on the model in Ref. [14] and Eq. (11) and disregard the layer compression term in the wavelength selection process. When the amplitude of the film undulation increases, the layer compression term prevents a further growth of strictly sinusoidal undulations. Then, the film deformation with period $2\pi/q$ becomes slightly more complex and has to be calculated by solving the Euler-Lagrange equation that minimizes the combined contributions of the K_{11} and B terms. We refrain from this calculation which is of little relevance here but mention that the limiting case where the layer compression term is completely avoided is a deformation where the film bends in alternating arcs with radii of curvature $R = \pm\pi^2/(8aq^2)$. For small amplitudes a, this function is quite similar to a sine shape. The splay elastic energy contribution of such a deformation would change to $32\pi^{-4}a^2q^4 \approx 0.328\,a^2q^4$ compared to the $0.25\,a^2q^4$ of the sine deformation of same periodicity and amplitude. Thus, we can tacitly ignore the layer compression term in our approximate model. It adds but a small numerical correction.

The growth rate of the wrinkle must be related to the surrounding airflow, from the crests to the valleys of the undulation, and consequently to the pressure profile along the island $p(r)$. Again, we approximate the airflow with a linear ansatz, neglecting the circular geometry, since we are primarily interested in a qualitative description of the instability mechanism. The pressure profile above the film inside the island may be approximated by $p(r) = p_0 \sin qr$. Therefore, the dissipated energy W_f in the radial geometry of the island may be assumed to be

$$W_f = \frac{\pi r^2}{2Cq^2} a\dot{a}, \qquad (13)$$

where $\dot{a} = da/dt$ The balance between the works, $W_s + W_d = W_\mathrm{f} + W_\mathrm{b}$, would lead to the dispersion relation

$$\dot{a} = \left(\left[(F_s + (\gamma/r))q^4 - K_{11}hq^6 \right] a \right) \frac{C}{2}, \qquad (14)$$

where we have omitted the layer compression term on the basis of the considerations above.

Since we are interested in a qualitative description of the instability mechanism, the radius r is approximated by a fixed value $r_c \approx 10^{-4}$ m corresponding to the experimental island radius at the onset of wrinkling. Eq. (14) describes the growth of a mode band between $q = 0$ and $q_c = \sqrt{(F_s + (\gamma/r_c))/(K_{11}h)}$. The fastest growing mode expected to select the wavelength value is found to be

$$q_\mathrm{max} = \sqrt{\frac{(F_s + (\gamma/r_c))}{2K_{11}h}}. \qquad (15)$$

VII. DISCUSSION

First, we establish a relation between the amplitude growth rate $\dot{a}$ and the island radius shrinkage rate Γ, using Eq. (3) and the experimental result of Fig. 7d through the relation

$$-\Gamma = \frac{\mathrm{d}(r_0 - r)}{\mathrm{d}t} \approx \frac{\mathrm{d}}{\mathrm{d}t} \frac{a^2 q_\mathrm{max}^2 r}{8} = \frac{a\pi^2 r}{\lambda^2}\dot{a}.$$

With the experimental value $r/\lambda \approx 2$ at onset (Fig. 7b), and an estimated amplitude $a \approx 0.1\lambda$ at the threshold of optical visibility of the patterns, one obtains $\dot{a} \approx |\Gamma/2| \approx 1\ \mu$m/ms at the time when the wrinkles become visible. Once the pattern is well established, the amplitude a of the wrinkles can be estimated from the ratio of the observed island radius r and the extrapolated r_0, using the data in Fig. 7 at 80 ms, as an example

$$a \approx \sqrt{\frac{8(r_0 - r)}{4\pi^2 r}}\lambda \approx 0.3\lambda.$$

which corresponds to amplitudes a of the order of 10 μm. In view of the optically well-recognized patterns, this result appears reasonable.

However, our model leads to a dilemma: In order to demonstrate this, let us estimate the value of $F_s + \gamma/r$ from Eq. 15 where for simplicity, we use an approximated fixed value of the island radius $r \approx r_c = 10^{-4}$ m. We transform this equation and use the relations $h = Nd_0$ (neglecting the background film thickness), $\gamma = N\gamma_s$ for N dislocations, and obtain

$$\gamma_s = q_\mathrm{max}^2 \cdot 2K_{11}d_0 r_c - F_s r_c/N. \qquad (16)$$

Substitution of the known values yields

$$\gamma_s = 8.6 \cdot 10^{-14}\ \mathrm{N} - F_s r_c/N \qquad (17)$$

Including a background film with a thickness of the same order of magnitude as the surplus island layers may increase the first term by a factor of about 2, but won't change its order of magnitude. The problem with this result is that γ_s has been measured by Géminard et al.

[59] for the smectic A material 4n-Octyl-4-cyanobiphenyl (8CB), from the distortion of thin regions in a vertical smectic film under gravitation. Their experiment is a 2D equivalent of the pendant drop method for the measurement of surface tensions. The line tension of the border around a region of reduced film thickness ('hole') is proportional to the Burgers vector of the dislocation. For a single dislocation, the line tension was found to be $\gamma_s \approx 10^{-11}$ N. Independent measurements of γ_s [48, 58] in different experimental configurations confirmed this value. It is more than two orders of magnitude larger than the first term on the right side of our estimate of Eq. (17). The second, negative term even increases this discrepancy.

In addition, if F_s was negligible compared to γ/r_c in Eq. (15), wrinkles within islands would be expected even without external bubble perturbations. This contradicts the experiment where a large number of islands display neither wrinkles nor bulges during the bubble shape relaxation.

We thus need to answer two questions. (I) How to reconcile the literature values of γ_s, which we have confirmed in independent experiments to be of the same order of magnitude for the present material [43], and the value of $(F_s + \gamma/r_c)$ derived from the measurements of the pattern wavelength and our modified wavelength selection model? (II) Why do islands in general remain flat if the system can gain energy by bulging the film inside, shortening the dislocations at practically constant surface area?

The answer to question (II) is easier. Most experiments with smectic freely suspended films have been carried out in fixed frames so far. In that situation, bulging of an island that shortens the island border requires the creation of additional film area outside the island. This process is inhibited by the surface tension of the material, which tends to preserve or reduce the film surface. Forces related to surface tension are in general much stronger than those mediated by the dislocations around islands. Thus, in all geometries with films that represent minimal surfaces in a fixed frame, islands remain flat. The same applies to spherical smectic bubbles on a capillary support, and to freely floating spherical bubbles. Wrinkling or bulging inside an island can occur only if the island can shrink without increasing the surface of the remaining film. That's why the phenomenon was so far only found in freely floating bubbles that have not yet reached their equilibrium sphere shape. The same can in principle be expected in a freely floating film of arbitrary shape with a free edge. Figure 12 demonstrates this in an example of an equilibrium spherical film and an adjacent freely floating film rag. This rag has a free border and thus it is rapidly shrinking to finally form a single droplet. Because of the free edges, islands on this non-equilibrium structure can form bulges and more complex protrusions without increasing the total film area. In contrast, islands on the bubble keep their flat shape.

Question (I) regarding the heavily overestimated contributions of line tension requires a new hypothesis. The experiments which led to the measurement of line tensions of dislocations are quasi-static. Géminard et al. [59] studied the equilibrium shapes of film holes under the combined actions of gravitation and line tensions of dislocations. They determined the stationary value of γ_s. The same applies to our unpublished measurements of γ_s in the present material: The line tension was determined from the final stage of coalescing islands on bubbles [43], and this process is also sufficiently slow so that one can use it as a good approximation for the static value of γ_s. It also applies to the line tension measurement and the corresponding model of the late stages of coalescence of Nguyen et al. [48]. However, the very early stages of island coalescence, where the local reduction rate of dislocation lengths is large, display clear discrepancies with the model based on an equilibrium line tension. Recordings at high spatial and temporal resolution even reveal an unexpected initial acceleration phase of the neck velocity [48]. In such short periods, the dislocations cannot contract quick enough because such longitudinal contractions require the rapid reconstruction of the local smectic layer structure. Nguyen et al. [48] suggested a global permeation out of the dislocations along the island perimeter. This resistance against a contraction of the dislocations leads to an effective reduction of the line tension, and vice versa it would result in an effectively increased line tension when the dislocations are stretched.

This means that we have to assume that the γ term introduced above is not the usual static line tension but an effective, dynamic one. This hypothesis needs to be tested in further experiments, but for now, it seems to be the only reasonable explanation of our experimental observations that (I) wrinkles and protrusions form in smectic islands under strong lateral compression of the local films, even if the surrounding film does not develop undulations, and (II) without film compression, the islands remain flat even if the bubbles have not yet reached their equilibrium sphere shape.

We have shown in Fig. 9 that islands can react to the local compression in different ways depending on their size. The large island shown by the blue square has the smallest value of γ/r_c, and in agreement with this it displays neither wrinkles nor a bulge. The smallest island enclosed in the red square experiences the highest stress of the three islands since γ/r_c is the largest. Such a small island, however, may not be suitable to accommodate wrinkles because its radius is not larger than the characteristic wavelength λ of wrinkles. Thus, the island bulges out of the film plane instead, as observed. This suggests that the selection of wrinkling or bulging scenarios at comparable external compression dynamics is dictated by the island size in comparison to the most unstable wrinkle wavelength.

The two types of wrinkles, star and ring shaped patterns, are structurally very similar to features observed in experiments on the formation of wrinkling

Figure 12. Closed bubble and freely floating film sheet, not in contact with each other. The islands in the bubble remain undistorted, while those in the floating film form bulges under comparable conditions. Image size 4 mm ×4 mm.

patterns atop shape memory polymers (Fig. 1) [37]. A thin gold elastic sheet lying on a soft substrate develops wrinkled patterns when subject to an external forcing or as a result of geometric incompatibility. Formation of similar wrinkling patterns has a quite different origin in solid sheets and smectic films, but it seems that the two phenomena have two features in common: First, the wrinkling is the consequence of the shrinkage of the circumference of the local patch, and second, the morphology of the pattern is controlled by the existence of a central protrusion. If such a protrusion exists, radial patterns are preferentially formed, and in absence of such protrusions the wrinkling pattern has a target structure. In any case, the patches are flattened again when the stress is relieved. A pronounced difference between the solid sheets and the smectic films is that for the solid sheets, the dynamics of the compression is of little relevance, whereas for the smectic films, a rapid compression is required. Otherwise, the films remain flat.

VIII. CONCLUSIONS

Dynamics of islands in freely floating smectic C bubbles have been investigated by means of high-speed video analysis, under zero-gravity conditions. It has been demonstrated that smectic films can behave similar to solid sheets under sufficiently fast and strong lateral compression. Wrinkling patterns observed within islands of larger film thickness are structurally equivalent to those of, e. g., thin gold films on a polymer substrate with incompatible thermal expansion coefficients under temperature changes. In smectic islands, these instabilities allow to compensate in-plane shrinkage under lateral compression and to accommodate in-plane compression stress with few surface reduction. When the deformation ceases, the wrinkles disappear and the island surface area remains approximately unchanged. Depending on the presence of a central protrusion in the island, the morphology of the wrinkles can be either a radial ray pattern or a target pattern, which is also similar to the observations in thin solid films. Similar instabilities have not been observed in conventional low-viscosity soap films because they do not generate islands surrounded by dislocations, and because they can instantaneously change their thickness and film area under strong lateral compression.

A dynamic model developed for the description of wrinkles in freely floating bubbles has been adapted to describe the wavelength selection in wrinkling islands. We discuss the role of the smectic layer compression coefficient which was neglected in the earlier model [14]. Layer compression can be avoided when the films undulate in circular arc segments instead of a sinusoidal shape. This leads only to a small numerical correction factor in the dynamic equations, which does not change the qualitative outcome noticeably. This layer compression effect, however, has dramatic influences on the shapes of protrusions that are formed in the centres of islands. The shapes of these protrusions (see Fig. 5) are composed of elements that contain cylindrical, conic, spherical and other segments that preserve the local smectic layer thickness. The protrusions prefer shapes that avoid the compression of smectic layers. A more detailed inspection of these patterns is desirable, but it requires a different observation technique with higher spatial resolution.

The model describing wrinkling islands suggests that the probability of forming wrinkles increases with smaller island radius as long as the most unstable wrinkle wavelength is smaller than the island radius. It also highlights the important role of the island line tension associated with the presence of the dislocations surrounding the islands. Comparison with experiments suggests that the dynamic line tension is significantly smaller than the static one.

Our observations may trigger further experiments where flat films in a reconfigurable frame are rapidly compressed by changing the frame area. This would allow a more quantitative access to wrinkling dynamics as a function of film thickness, island diameters and compression speeds, because the film geometry can then be adjusted before the compression experiment without the need of a catenoid collapse. In the latter, one has no control of the formation of islands or film thicknesses and only limited control of the compression dynamics.

ACKNOWLEDGMENTS

This study was funded by DFG with projects STA 425/40 and HA8467/2-1 and by DLR within project 50WM2054. AM thanks the Centre National d'Etudes Spatiales (CNES) that allowed him to pursue his PHD. CNES is also aknowledged to have allowed for microgravity experiments (VP148 CNES parabolic flight campaign) operated by Novespace (Bordeaux, France).

We thank the staff of Novespace for their technical support during the parabolic flight campaigns.

[1] L. Rayleigh, *The Theory of Sound*, Macmillan and Co., London, 1894.
[2] L. D. Landau and E. M. Lifschitz, *Hydrodynamik*, Akademie Verlag, Berlin, 1993.
[3] H. Lamb, *Hydrodynamics*, Dover, New York, 1932.
[4] C. A. Miller and L. E. Scriven, *J. Fluid Mech.*, 1968, **32**, 417–435.
[5] A. Prosperetti, *J. Fluid Mech.*, 1980, **100**, 333–347.
[6] P. L. Marston and R. E. Apfel, *J. Acoust. Soc. Am.*, 1980, **67(1)**, 27–37.
[7] U. Kornek, F. Müller, K. Harth, A. Hahn, S. Ganesan, L. Tobiska and R. Stannarius, *New J. Phys.*, 2010, **12**, 073031.
[8] P. Grinfeld, *Stud. Appl. Math.*, 2012, **128**, 30–39.
[9] P. Grinfeld, *Phys. Rev. Lett.*, 2010, **105**, 137802.
[10] K. May, K. Harth, T. Trittel and R. Stannarius, *Europhys. Lett.*, 2012, **100**, 16003.
[11] K. May, K. Harth, T. Trittel and R. Stannarius, *ChemPhysChem*, 2014, **15**, 1508.
[12] K. Harth, *Ph.D. thesis*, Otto von Guericke University, Magdeburg, Germany, 2016.
[13] P. Dähmlow, T. Trittel, K. May, K. Harth and R. Stannarius, *Liquid Crystals*, 2018, **45**, 993.
[14] K. Harth, T. Trittel, K. May and R. Stannarius, *Soft Matter*, 2019, **15**, 6769–6778.
[15] P. C. Petit, M. L. Merrer and A.-L. Biance, *J. Fluid Mech.*, 2015, **774**, R3.
[16] W. R. McEntee and K. J. Mysels, *J. Phys. Chem.*, 1969, **73**, 3018–3028.
[17] R. da Silveira, S. Chaieb and L. Mahadevan, *Science*, 2000, **287**, 1468–1471.
[18] E. Q. Li, D. Beilharz and S. T. Thoroddsen, *Phys. Rev. Fluids*, 2017, **2**, 073602.
[19] M. L. Merrer, D. Quéré and C. Clanet, *Phys. Rev. Lett.*, 2012, **109**, 064502.
[20] S. M. Salili, T. Ostapenko, O. Kress, C. Bailey, W. Weissflog, K. Harth, A. Eremin, R. Stannarius and A. Jákli, *Soft Matter*, 2016, **12**, 4725.
[21] F. Jähnig, *Biophys. J.*, 1996, **71**, 1348–1349.
[22] V. Kantsler, E. Segre and V. Steinberg, *Phys. Rev. Lett.*, 2007, **99**, 178102.
[23] M. Staykova, D. P. Holmes, C. Read and H. A. Stone, *PNAS*, 2011, **108**, 9084–9088.
[24] L. Wang, C. E. Castroac and M. C. Boyce, *Soft Matter*, 2011, **7**, 11319–11324.
[25] K. Liu, C. Hamilton, J. Allard, J. Lowengrub and S. Li, *Soft Matter*, 2016, **12**, 5663.
[26] E. Cerda and L. Mahadevan, *Phys. Rev. Lett*, 2003, **90**, 074302.
[27] Z. Liu, N. Fujita, O. Terasaki, T. Ohsuna, K. Hiraga, M. A. Camblor, M. D. Cabanas and A. K. Cheetham, *Chemistry*, 2002, **8**, 4549–4556.
[28] D. Vella, A. Ajdari, A. Vaziri and A. Boudaoud, *Phys. Rev. Lett.*, 2011, **107**, 174301.
[29] J. Huang, B. Davidovitch, C. D. Santangelo, T. P. Russell and N. Menon, *Phys. Rev. Lett.*, 2010, **105**, 038302.
[30] M. Pineirua, N. Tanaka, B. Roman and J. Bico, *Soft Matter*, 2013, **9**, 10985.
[31] H. Vandeparre, M. Pineirua, F. Brau, B. Roman, J. Bico, C. Gay, W. Bao, C. N. Lau, P. M. Reis and P. Damman, *Phys. Rev. Lett.*, 2011, **106**, 224301.
[32] O. Tovkach, J. Chen, M. M. Ripp, T. Zhang, J. D. Paulsen and B. Davidovitch, *PNAS*, 2020, **117**, 3938–3943.
[33] S. Yu, Y. Sun, X. Zhang, C. Lu, H. Zhou and Y. Ni, *Phys. Rev. E*, 2019, **99**, 062802.
[34] J. D. Paulsen, *Annu. Rev. Cond. Mat. Phys.*, 2019, **10**, 431–450.
[35] F. Box, D. O'Kiely, O. Kodio, M. Inizan, A. A. Castrejón-Pita and D. Vella, *PNAS*, 2019, **116**, 20875–20880.
[36] J. Y. Chung, A. J. Nolte and C. M. Stafford, *Adv. Mater.*, 2009, **21**, 1358.
[37] Y. Zhao, W. M. Huang and Y. Q. Fu, *J. Micromech. Microeng.*, 2011, **21**, 067007.
[38] C. Klopp, T. Trittel, K. Harth and R. Stannarius, *Soft Matter*, 2022, **18**, 146–155.
[39] J. Huang, M. Juszkiewicz, W. H. de Jeu, E. Cerda, T. Emrick, N. Menon and T. P. Russell, *Science*, 2007, **317**, 650.
[40] F. Müller and R. Stannarius, *Europhys. Lett.*, 2006, **76**, 1102–1108.
[41] N. D. Robinson and P. H. Steen, *J. Coll. Int. Sci.*, 2001, **241**, 448–458.
[42] R. Stannarius, C. Cramer and H. Schüring, *Mol. Cryst. Liq. Cryst.*, 1999, **329**, 1035.
[43] K. Harth, A. Missaoui, T. Trittel, E. Lacaze and R. Stannarius, in preparation.
[44] E. Enz, *Ph.D. thesis*, Martin-Luther-Universität Halle-Wittenberg, Halle, Germany, 2013.
[45] T. Trittel, K. Harth and R. Stannarius, *Soft Matter*, 2017, **13**, 3199.
[46] N. A. Clark, A. Eremin, M. A. Glaser, N. R. Hall, K. Harth, C. Klopp, J. E. Maclennan, C. S. Park, R. Stannarius, P. Tin, W. N. Thurmes and T. Trittel, *Adv. Space Res.*, 2017, **60**, 737.
[47] D. H. Nguyen, *Smectic liquid crystal freely suspended films: Testing beds for the physics in thin membranes*, 2011.
[48] Z. H. Nguyen, K. Harth, A. M. Goldfain, C. S. Park, M. A. G. J. E. Maclennan and N. A. Clark, *Phys. Rev. Research*, 2021, **3**, 033143.
[49] N. S. Shuravin, P. V. Dolganov and V. K. Dolganov, *Phys. Rev. E*, 2019, **99**, 062702.
[50] J. C. Loudet, P. V. Dolganov, P. Patricio, H. Saadaoui and P. Cluzeau, *Phys. Rev. Lett.*, 2011, **106**, 117802.
[51] K. Harth, B. Schulz, C. Bahr and R. Stannarius, *Soft Matter*, 2011, **7**, 7103–7111.
[52] K. Harth, A. Eremin and R. Stannarius, *Ferroelectrics*, 2012, **431**, 59.
[53] N. V. Maduhusudana, *Phys. Rev. E*, 2020, **102**, 032701.
[54] H. Helfrich, *Appl. Phys. Lett.*, 1970, **17**, 531.
[55] J. P. Hurault, *J. Chem. Phys.*, 1973, **59**, 2068.
[56] M. Delaye, R. Ribotta and G. Durand, *Physics Letters A*, 1973, **44**, 139.

[57] C. Blanc, G. Durey, R. D. Kamien, T. Lopez-Leon, M. O. Lavrentovich and L. Tran, *Helfrich-Hurault elastic instabilities driven by geometrical frustration*, 2021, ariv:2109.14668v1.

[58] L. Zou, J. Wang, P. Basnet and E. K. Mann, *Phys. Rev. E*, 2007, **76**, 031602.

[59] J.-C. Géminard, C. Laroche and P. Oswald, *Phys. Rev. E*, 1998, **58**, 5923–5925.